



Research paper

Hierarchical Z-scheme photocatalyst of g-C₃N₄@Ag/BiVO₄ (040) with enhanced visible-light-induced photocatalytic oxidation performanceMan Ou^{a,b}, Shipeng Wan^{a,b}, Qin Zhong^{a,b,*}, Shule Zhang^{a,b}, Yang Song^{a,b}, Lina Guo^{a,b}, Wei Cai^c, Yalin Xu^{a,c}^a School of Chemical Engineering, Nanjing University of Science and Technology Nanjing, Jiangsu 210094, PR China^b Nanjing AIREP Environmental Protection Technology Co., Ltd, Nanjing, Jiangsu 210091, PR China^c Jiangsu Collaborative Innovation Center of Atmospheric Environment and Equipment Technology (CICAET), Nanjing University of Information Science & Technology, Jiangsu Key Laboratory of Atmospheric Environment Monitoring and Pollution Control (AEMPC), Nanjing, Jiangsu 210044, PR China

ARTICLE INFO

Keywords:

Facets

g-C₃N₄@Ag/BiVO₄

Z-Scheme

Photocatalytic oxidation

ABSTRACT

The preferred exposure of (040) crystal facet of BiVO₄ is conducive to optimizing its photocatalytic performance. And the great separation of photoinduced electron-hole pairs is also a critical factor for semiconductor photocatalyst. Herein we designed a hierarchical g-C₃N₄@Ag/BiVO₄ (040) hybrid photocatalyst, in which Ag was photodeposited on the (040) facets of BiVO₄ and subsequently g-C₃N₄ was covered on the surface of Ag/BiVO₄ (040). The physical and chemical properties of the synthetic samples were analyzed by several characterization techniques. SEM spectrum clearly reveals the morphology and structure of g-C₃N₄@Ag/BiVO₄ (040), suggesting the existence of the hierarchical composite photocatalyst. The visible light absorption wavelength of the composite is increased due to the surface plasmon resonance (SPR) effect of metal Ag nanoparticles, displayed in UV–vis spectrum. The photogenerated electron-hole pairs are also greatly enhanced through the Z-scheme g-C₃N₄@Ag/BiVO₄ (040) system with the Ag nanoparticles as the electron mediator. The above synergistic effects of the hybrid photocatalyst result in higher photocatalytic oxidation performance not only for water splitting but also for NO oxidation in gas phase compared with pure BiVO₄.

1. Introduction

Semiconductor heterogeneous photocatalysis has been received keen interest in recent years to solve global energy crisis and natural environments deterioration [1,2]. The development of highly active photocatalysts remains a huge undertaking. Previously, we reported the monoclinic BiVO₄ with strong photo-oxidation properties, which could efficiently oxidize high concentration NO (~400 ppm) with the help of H₂O₂ under visible light irradiation [3,4]. The strong oxidizing property of BiVO₄ is ascribed to its positive valence band value ($E_{VB} = 2.7$ eV) [5]. The excellent property triggers us to investigate its effects on the oxidation of water to produce O₂ (E_0 (H₂O/O₂) = 1.23 eV) [6] and NO in flue gas to NO₃[−] (E_0 (HNO₃/NO) = 0.94 eV) [7] under visible light irradiation, making the material possess versatility.

Theoretical and experimental research have demonstrated that the surface of monoclinic BiVO₄ (040) facets can provide more multi-atomic centers BiV₄, which is the origin of the multi-electron transfer and then served as active sites in the photocatalytic reaction [8]. Thus, it's worth constructing the BiVO₄ material with a high proportion of

(040) facets. However, the photocatalytic performance of the single BiVO₄ can be also limited by its low separated rate of photogenerated charge carriers. In order to resolve this problem, many efforts such as doping with nonmetallic [9], combined with graphene [10,11] and constructing heterojunctions [12–14] with two semiconductors have been carried out. Therein, the heterojunction photocatalyst usually displays the higher photoactivity since it is able to facilitate the separation of photogenerated charge carriers to a large extent, and then leaving more electrons and holes participating in the photocatalytic reaction.

Among the numerous heterojunction photocatalysts, the Z-scheme photocatalytic system possesses the potential to achieve larger separation ratio of photo-induced electrons and holes. Generally speaking, the artificial heterogeneous Z-scheme consists of two different semiconductor photocatalysts with suitable band gaps and an electron mediator. In recent years, the noble-metal, such as Au, Pt and Ag were mainly adopted as the electron mediator to transport electrons to improve the photoactivity [15–18]. Zhao et al. constructed an all-solid-state g-C₃N₄/Au/P25 Z-scheme photocatalyst for visible-light-driven H₂

* Corresponding author at: School of Chemical Engineering, Nanjing University of Science and Technology Nanjing, Jiangsu 210094, PR China.
E-mail address: zq304@mail.njust.edu.cn (Q. Zhong).

evolution, and the Z-scheme sample exhibited higher photocatalytic performance with respect to pure g-C₃N₄. It was attributed to the effective electron transfer and separation rate of photo-induced electron-hole pairs caused by the vectorial electron transfer of P25 → Au → g-C₃N₄ [17]. The Z-scheme BiVO₄-Ru/SrTiO₃:Rh photocatalyst was synthesized for water splitting under visible light irradiation, which also displayed higher photocatalytic performance than the single component [14]. g-C₃N₄ is also a narrow band gap semiconductor with the CB position at ca. −1.3 eV and the VB position at ca. 1.4 eV vs NHE, which can match well with the BiVO₄ with exposed (040) facets to form an Z-scheme photocatalytic system [19,20]. In addition, Ag as relatively cheap noble metal can usually be selected as the “linker” to shuttle the electrons between the two semiconductor components in Z-scheme [18,21]. Up to now, some studies about the g-C₃N₄/Ag/BiVO₄ ternary composite [22,23] have been reported, but relative reports about the BiVO₄ (040)-based ternary materials were quietly scarce. And in the application filed, the g-C₃N₄/Ag/BiVO₄ photocatalysts were usually used in the aqueous phase for decomposition and decolorization of organics, and few ternary composite photocatalyst was used for photocatalytic water oxidation to O₂ and photocatalytic oxidation of NO in gas phase to NO₃[−].

Herein, the g-C₃N₄@Ag/BiVO₄ (040) sample was synthesized in this work to construct a hierarchical hybrid photocatalyst, in which the linker metal Ag was photo-deposited on the (040) crystal facet of BiVO₄ and the g-C₃N₄ prepared by supramolecular method was wrapped the Ag/BiVO₄ (040) by a facile reflux method. The photocatalytic performance of the g-C₃N₄@Ag/BiVO₄ (040) composite was focused on photocatalytic oxidation of water to O₂ and NO in gas phase to NO₃[−]. The photocatalytic properties of the hierarchical hybrid photocatalyst were also evaluated by the structure, electronic environment and optical properties. The enhanced ability of the photocatalytic oxidation was remarkable, and reasons were discussed. As well, in this paper, the detailed mechanism of the photocatalysis over Z-scheme g-C₃N₄@Ag/BiVO₄ (040) sample was also further clarified and discussed.

2. Experimental

2.1. Preparation of g-C₃N₄@Ag/BiVO₄ (040) hybrid photocatalyst

2.1.1. Preparation of BiVO₄ sample

BiVO₄ sample with dominant exposed (040) facets was synthesized by a previously reported method [24]. Typically, 6 mmol Bi(NO₃)₃·5H₂O was well dispersed into HNO₃ (2 mol/L, 13.5 mL) aqueous solution under vigorous stirring until a clear solution was formed (A). Meanwhile 6 mmol NH₄VO₃ was dissolved in HNO₃ (2 mol/L, 36.5 mL) aqueous solution with ultrasonic process to form a yellowish orange transparent solution (B). Subsequently, the B solution was added dropwise into the A solution with mechanical agitation. The pH value was adjusted into about 2 by the NH₃·H₂O and subsequently the salmon precipitation was observed. After being stirred for 30 min, the precursor solution was transferred into a 100 mL Teflon-lined stainless steel autoclave and maintained at 200 °C and autogenous pressure for 24 h. After the autoclave was cooled down to room temperature, the precipitation was collected by centrifugation, washed by deionized water and absolute alcohol for several times, and then dried at 80 °C overnight. The product obtained was denoted BiVO₄.

2.1.2. Photo-deposition of Ag on BiVO₄ (040) facets

The photoexcited electrons of BiVO₄ photocatalyst under light irradiation have been

demonstrated to be driven to (040) facets of BiVO₄ [24]. Here, the photo-deposition of the Ag on (040) facets of BiVO₄ was achieved with AgNO₃ as the precursor, methanol was employed as the hole scavenger. Typically, BiVO₄ (0.4 g), AgNO₃ (12.6 mg) and 4 mL methanol was successively added to 40 mL deionized water under magnetic stirring. Subsequently, the obtained yellow mixture was irradiated by 350 W Xe

light (λ > 420 nm) for 2 h. The color of the solution turned from vivid yellow to grayish-green, which suggested the generation of Ag species in reaction system. Finally, the obtained 2 wt% Ag/BiVO₄ product was centrifuged and dried at 80 °C at vacuum oven for overnight. Then the nominal 1 wt% Ag/BiVO₄ and 3 wt% Ag/BiVO₄ photocatalysts were also prepared. If there is no special requirement, Ag/BiVO₄, as it mentions in the paper, refers to 2 wt% Ag loading on the surface of BiVO₄ (040) facets.

2.1.3. Preparation of g-C₃N₄@Ag/BiVO₄ (040) sample

The floccular g-C₃N₄ was synthesized as follows: 0.8 mmol cyanuric acid, 0.4 mmol melamine and 0.4 mmol 2,4-diamino-6-methyl-1,3,5-triazine were mixed in 100 mL deionized water, and vigorously stirred for 12 h to make sure a reiterative dynamic dissolution to allow the formation of crystalline supramolecular complex. Then the milky suspension was centrifuged and washed with deionized water several times. The resulting powders were dried at 60 °C overnight under vacuum conditions and calcined at 550 °C for 4 h at a heating rate of 2 K min^{−1} under N₂ atmosphere.

The g-C₃N₄@Ag/BiVO₄ (040) sample was prepared by a reflux method. An appropriate amount of floccular g-C₃N₄ and Ag/BiVO₄ (040) sample were added to 50 mL deionized water, and then the mixture was obtained by a reflux reaction at 90 °C for 3 h. The obtained g-C₃N₄@Ag/BiVO₄ (040) photocatalyst was washed with water, and finally dried in an oven at 80 °C overnight. The obtained photocatalysts with different mass ratios of g-C₃N₄ were named as 50% g-C₃N₄@Ag/BiVO₄, 100% g-C₃N₄@Ag/BiVO₄ and 150% g-C₃N₄@Ag/BiVO₄. And unless otherwise noted, g-C₃N₄@Ag/BiVO₄, as it appears in the paper, represents the 100% g-C₃N₄@Ag/BiVO₄ sample. The photocatalyst g-C₃N₄@BiVO₄ was also prepared via the same process, but replacing Ag/BiVO₄ with BiVO₄.

2.2. Characterizations

The structural and chemical information for prepared samples were measured by X-ray diffraction (XRD, Cu Kα, Purkinjie XD-3), Fourier transform infrared (FT-IR) spectroscopy (Nicolet IS10, USA), Field-emission scanning electron microscope (SEM, FEI Quanta 250F), Brunauer-Emmett-Teller (BET, Quantachrome, autosorb IQ), X-ray photoelectron spectroscopy (XPS, PHI-5000C ESCA), UV-vis diffuse reflectance spectrum (DRS, Shimadzu UV-2600), Photoluminescence spectrum (PL, He-Cd laser, Labram-HR800), Electron paramagnetic resonance (EPR, Bruker EMX-10/12-type spectrometer).

The Mott-Schottky measurements were performed on a CHI 760D electrochemical workstation (shanghai Chenhua, China) using a standard three-electrode cell with a working electrode, a Pt wire as counter electrode, and a standard Ag/AgCl in saturated KCl as reference electrode. An aqueous solution of 0.5 mol/L Na₂SO₄ (pH 6.8) was used as electrolyte and purged with N₂ prior to each experiment. The working electrode was prepared by dip-coating: 10 mg photocatalyst was added into 1 mL ethyl alcohol and 50 μL Nafion solution to form slurry, and then dip-coated onto a 1 cm × 1 cm FTO glass electrode. Subsequently, the films were dried at 80 °C overnight and calcined at 180 °C for 2 h at N₂ atmosphere. The variations of photoinduced current density with time (*i*-*t* curve) and electrochemical impedance spectroscopies (EIS) were measured with a 350 W Xe light (with 420 nm filter) as the light source and 0.5 mol/L Na₂SO₄ as the electrolyte.

2.3. The photocatalytic oxidation reaction

2.3.1. The photocatalytic water oxidation

The photocatalytic O₂ evolution tests (Labsolar-III A1, Perfect Light, China) were carried out in NaIO₃ aqueous solution under visible light from 350 W Xe light equipped with a 420 nm cut filter. In each experiment, 90 mg photocatalyst was dispersed in 90 mL NaIO₃ aqueous solution (0.2 M) in a 200 mL reactor with a top window made of Pyrex at

room temperature. Prior the test, the photo-reaction system was bubbled by N_2 for 30 min to thoroughly remove the dissolved oxygen. The photocatalytic O_2 evolution were sampled at 20 min intervals during the irradiation and analyzed by an online gas chromatography with a thermal conductivity detector (GC7806).

2.3.2. The photocatalytic activity test (oxidation of NO)

The experiments for the photocatalytic oxidation (PCO) of NO were conducted at room temperature and atmospheric pressure in a fixed bed continuous flow tubular quartz reactor ($d = 1$ cm, $h = 15$ cm). The 350 W Xe-lamp was vertically placed, parallel with the reactor and a 420 nm cut-off filter was also placed. Photocatalyst (0.2 g) was carefully deposited on the inner walls of the reactor from a suspension of finely ground power in distilled water. After deposition, the reactor was dried at 100 °C overnight to remove the water. The mixture of reactant gases (400 ppm NO, 7% O_2/N_2 balance) was fed into the reactor with a total flow rate of 100 mL min⁻¹. In order to provide more active species for the PCO of NO and reduce the accumulation of reaction products on the surface of photocatalysts, 30% H_2O_2 solution was injected into the reactor with a flow rate of 0.02 mL min⁻¹. After the system was stable for 60 min, when there was no difference between the concentration of outlet NO and that of inlet gas, the lamp was turned on and the experiment started. The gas products (every 10 min reaction) were analyzed by an Ecom-JZKN flue gas analyzer (Germany) for 150 min under visible-light irradiation. The reaction of NO with O_2 was ignorable. The NO removal ratio is calculated by $NO \text{ conversion} = (NO_{in} - NO_{out}) / NO_{in} \times 100\%$.

3. Results and discussion

3.1. Photocatalytic oxidation performance

3.1.1. Photocatalytic water oxidation

The photocatalytic water oxidation performance of the prepared photocatalysts was measured for 6 h under visible light ($\lambda > 420$ nm) irradiation in the presence of $NaIO_3$ as a sacrificial electron acceptor. The control experiment without sample was conducted and nearly no O_2 was evolved. As shown in Fig. 1a, a negligible amount of O_2 was evolved for $g-C_3N_4$ (2.0 μmol in 6 h), while the O_2 amount was 7.4 μmol for pure $BiVO_4$, indicating that the single component showed little photocatalytic activity under visible light irradiation. The photocatalytic water oxidation of $Ag/BiVO_4$ with different content of metallic Ag was also conducted, as shown in Fig. S1a. The photocatalytic O_2 evolution of 1 wt% $Ag/BiVO_4$, 2 wt% $Ag/BiVO_4$ and 3 wt% $Ag/BiVO_4$ were 10.6, 16.5 and 13.7 μmol in 6 h, respectively. Based on the photocatalytic performance, 2 wt% Ag was the optimal photodeposition content, called as $Ag/BiVO_4$. Moreover, after the $g-C_3N_4$ wrapped the $Ag/BiVO_4$ sample, the photocatalytic oxidation activity was greatly enhanced. The O_2 concentration of 50% $g-C_3N_4@Ag/BiVO_4$, 100% $g-C_3N_4@Ag/BiVO_4$ and 150% $g-C_3N_4@Ag/BiVO_4$ was 57.4, 88.1 and 70.0 μmol in 6 h, respectively, shown in Fig. S1b. According to the above reports, the 100% $g-C_3N_4@Ag/BiVO_4$ composite photocatalyst with 2 wt% Ag content ($g-C_3N_4@Ag/BiVO_4$) displayed the highest photocatalytic oxidation performance. The photocatalytic water oxidation performance of the $BiVO_4$ -based samples modified by 2 wt% Ag or 100% $g-C_3N_4$ was depicted in Fig. 1a. Regarding the binary composite $g-C_3N_4@BiVO_4$ (100% $g-C_3N_4@BiVO_4$), small amounts of O_2 were evolved, which was 34.9 μmol . The phenomenon exhibited that the modification of Ag or $g-C_3N_4$ to $BiVO_4$ was conducive to the photocatalytic performance. The photocatalytic water oxidation process involves two reactions. One is the reduction of IO_3^- , and the other is the oxidation of water. The corresponding equations are listed as follows [24]:

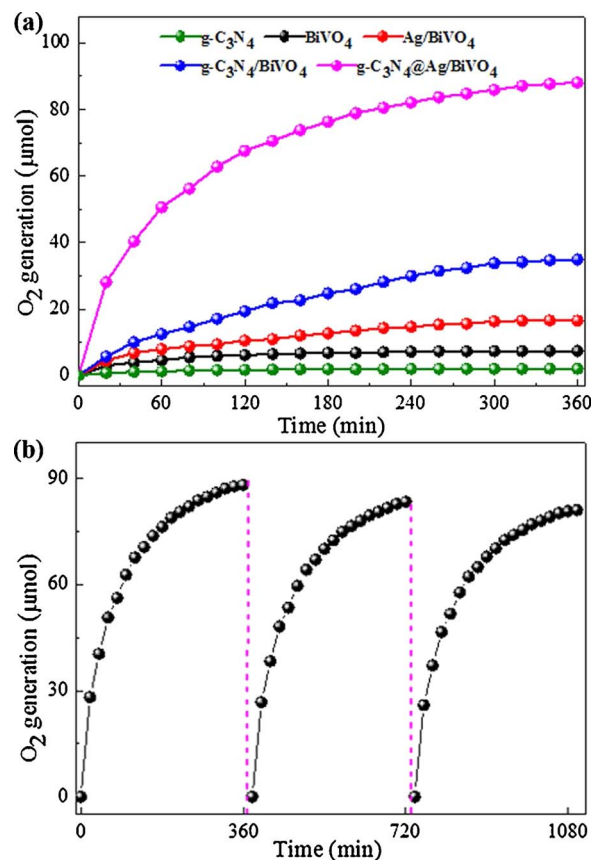
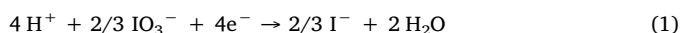


Fig. 1. (a) The photocatalytic evolution of O_2 from water over the $g-C_3N_4$, $BiVO_4$, $Ag/BiVO_4$, $g-C_3N_4@BiVO_4$ and $g-C_3N_4@Ag/BiVO_4$ photocatalysts; (b) Three-recycled photocatalytic water oxidation activities over $g-C_3N_4@Ag/BiVO_4$ photocatalyst. Reaction conditions: in all cases, the amount of photocatalysts was set to be 90 mg in 90 mL 0.02 M $NaIO_3$ aqueous solution, light source: 300 W Xe light ($\lambda \geq 420$ nm), top irradiation, reaction time: 6 h.



The increased O_2 content for binary photocatalysts was probably attributed to the more separated electrons and holes participating in the photocatalytic reaction. For $Ag/BiVO_4$, the photoinduced electrons on $BiVO_4$ (040) facets under visible light irradiation can be conducted via metal phase Ag, thus reducing the recombination ratio of photoinduced electrons and holes. For $g-C_3N_4@BiVO_4$ sample, the $g-C_3N_4@BiVO_4$ heterojunction might be formed due to the suitable band position [20]. The electrons on the conduction band of $g-C_3N_4$ will be injected into that of $BiVO_4$, meanwhile the holes on the valence band of $BiVO_4$ will be transferred to that of $g-C_3N_4$ under visible light irradiation, thereby the photoinduced electrons-holes separation will be greatly improved. After combining $Ag/BiVO_4$ (040) with $g-C_3N_4$, the results showed that the ternary composite photocatalyst $g-C_3N_4@Ag/BiVO_4$ displayed the highest photocatalytic water oxidation performance. It demonstrated that $g-C_3N_4@Ag/BiVO_4$ ternary photocatalyst possessed the largest number of photoinduced electrons-holes pairs which subsequently involved in the reduction of IO_3^- and oxidation of water, respectively. The reason for the difference of photocatalytic water oxidation of the $BiVO_4$ -based samples modified by different content of metallic Ag or $g-C_3N_4$ is also ascribed to the separated ratio of the photoinduced electrons and holes, which will be illustrated in the following $i-t$ and EIS measurements.

The photostability of $g-C_3N_4@Ag/BiVO_4$ hybrid photocatalyst was evaluated by measuring the recycled sample three times. After each test, the used sample was centrifuged and washed with deionized water three times and dried for the next recycled photoactivity test. After

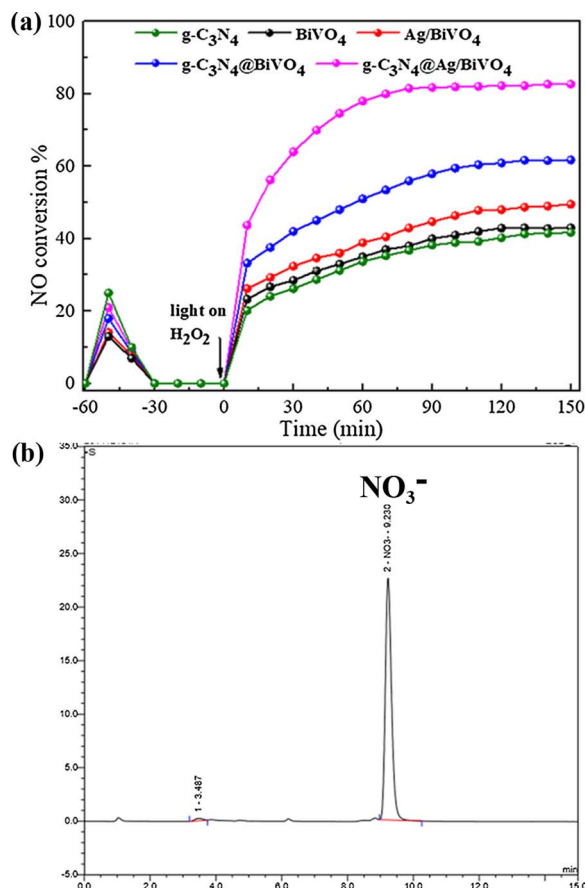


Fig. 2. (a) Variations of NO conversion efficiency with irradiation time for the as-synthesized g-C₃N₄, BiVO₄, Ag/BiVO₄, g-C₃N₄@BiVO₄ and g-C₃N₄@Ag/BiVO₄ photocatalysts; (b) Ion Chromatography analysis of reaction products after the photocatalytic reaction in the presence of g-C₃N₄@Ag/BiVO₄ for 150 min.

three photocatalytic cycles, the O₂ emission content was 81 μmol (Fig. 1b) with 8% decrease, suggesting the synthesized g-C₃N₄@Ag/BiVO₄ sample exhibited good efficiency and photostability. A slight O₂ concentration decline might result from the loss of the photocatalyst by centrifugation.

3.1.2. The enhanced photocatalytic activity of NO oxidation

Fig. 2 shows the photocatalytic oxidation (PCO) of NO ability of the hybrid photocatalysts. The adsorption-desorption process of NO on the catalyst surface in the first 60 min was conducted. And after that the Xe-lamp and the peristaltic pump that delivers the H₂O₂ solution were turned on. The variations of NO concentration with irradiation time over pure g-C₃N₄, BiVO₄, binary Ag/BiVO₄ and g-C₃N₄@BiVO₄ and ternary g-C₃N₄@Ag/BiVO₄ samples under visible light irradiation were shown in Fig. 2a. NO oxidation ratios could be negligible in the absence of visible light irradiation, photocatalyst or H₂O₂ solution and the control experimental results might be seen in our previous paper [4]. The NO concentration over the samples decreased gradually by photocatalytic oxidation, and the removal ratio of NO is 41%, 43%, 50%, 62% and 83% in 150 min in the presence of g-C₃N₄, BiVO₄, Ag/BiVO₄, g-C₃N₄@BiVO₄ and g-C₃N₄@Ag/BiVO₄ samples, respectively. Moreover, the PCO of NO of BiVO₄ photodeposited by different Ag content was also tested, as shown in Fig. S2a. The removal efficiency of NO over 1 wt% Ag/BiVO₄, 2 wt% Ag/BiVO₄ and 3 wt% Ag/BiVO₄ is 45%, 50% and 47% in 150 min, respectively. With the introduction of g-C₃N₄, the PCO of NO was increased extremely, which the NO removal rate over 50% g-C₃N₄@Ag/BiVO₄, 100% g-C₃N₄@Ag/BiVO₄ and 150% g-C₃N₄@Ag/BiVO₄ was 62%, 83% and 69%, respectively, in 150 min under visible light irradiation (Fig. S2b). The PCO of NO ability for the

synthetic samples was consistent with that of photocatalytic water oxidation performance. Overall, ternary g-C₃N₄@Ag/BiVO₄ hybrid photocatalyst exhibited higher photocatalytic oxidation performance compared with pure or binary photocatalysts.

In the experimental process of PCO of NO, NO could react with the free radicals (h⁺, ·OH, ·O₂⁻) to produce NO₂ and ionic species (NO₂⁻, NO₃⁻). In our experimental process, the increased amount of NO₂ was not detected, which illustrated that NO₂ was not the product. The used g-C₃N₄@Ag/BiVO₄ photocatalyst was submerged into the deionized water for overnight and then centrifuged to inject the supernatant into Ion Chromatography (DionexICS90). The obtained result indicated that the major product of PCO of NO was NO₃⁻, as shown in Fig. 2b. The involved possible reactions were as follows in the process of the PCO of NO [25].



3.2. Structural and chemical characterizations

The phase, crystallite structure and crystal perfection of photocatalyst samples were determined by XRD analyses. Fig. 3 displays the XRD patterns of g-C₃N₄@Ag/BiVO₄ hybrid photocatalyst with those g-C₃N₄, BiVO₄, Ag/BiVO₄ and g-C₃N₄@BiVO₄. It can be observed that all the peaks of BiVO₄ based photocatalysts can be well-indexed as the standard monoclinic BiVO₄ with a space group of I2/a (JCPDS NO. 14-

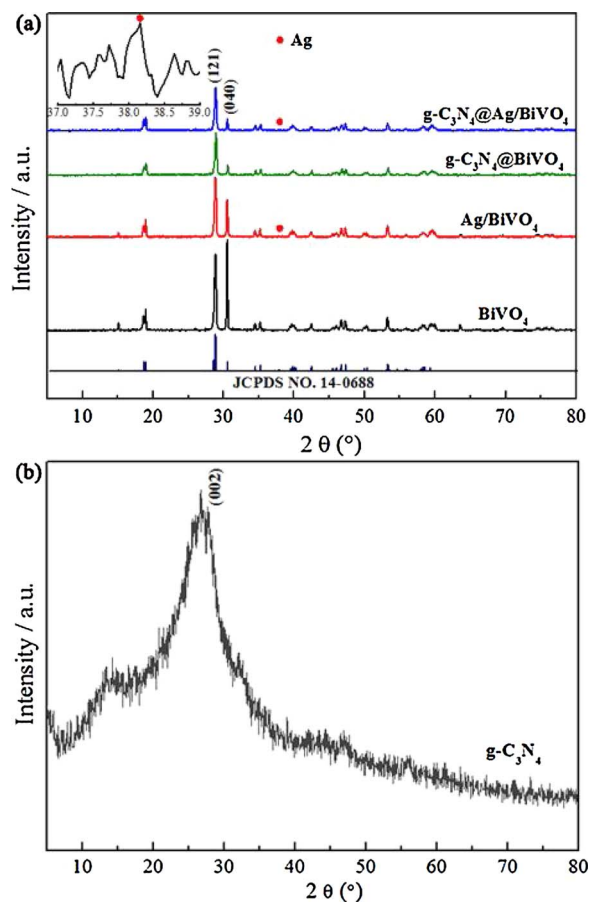


Fig. 3. XRD patterns of (a) BiVO₄, Ag/BiVO₄, g-C₃N₄@BiVO₄ and g-C₃N₄@Ag/BiVO₄ and (b) pure g-C₃N₄.

0688) [26]. After deposition of Ag nanoparticles, the characterization peak of Ag at 38.1° [21] is detected from XRD pattern of Ag/BiVO₄ and g-C₃N₄@Ag/BiVO₄ (Fig. 3 inset). The peak at $2\theta = 27^\circ$ in pure g-C₃N₄ indexed as (002) peaks is due to the interlayer-stacking of aromatic systems as in graphite [27], as shown in Fig. 3b. No obvious peaks of g-C₃N₄ phase are observed in the patterns of g-C₃N₄@BiVO₄ and g-C₃N₄@Ag/BiVO₄, which may be a result of the low diffraction intensity. The XRD results indicate that the crystalline and structure of BiVO₄ in the hybrid photocatalysts do not change and no other impurities are observed. The main difference in the observed patterns pertains to the intensity of the (040) peak. It is worth noting that the relative intensity of the diffraction peaks (I_{040}/I_{121}) shrinks notably after the addition of Ag or g-C₃N₄. It suggests that the (040) facets of BiVO₄ was successfully deposited by Ag or enwrapped by g-C₃N₄, which can be intuitively seen in the following SEM images. For g-C₃N₄@Ag/BiVO₄ hybrid photocatalyst, Ag was first deposited on (040) facets of BiVO₄, and then covered by g-C₃N₄. Therefore, the hierarchical g-C₃N₄@Ag/BiVO₄ hybrid photocatalyst, in which Ag nanoparticles act as the “linker” between BiVO₄ (040) and g-C₃N₄, has been obtained.

A comparison of FT-IR spectrum of BiVO₄, g-C₃N₄, Ag/BiVO₄, g-C₃N₄@BiVO₄ and g-C₃N₄@Ag/BiVO₄ photocatalysts is shown in Fig. S3. The band located at 741 cm^{-1} belongs to the bending vibration band of V-O group [28]. After the Ag was photodeposited on the surface of BiVO₄ (040) facets, no other new bands are observed, due to the low amount of metallic Ag in Ag/BiVO₄ sample. In the FT-IR spectrum of g-C₃N₄, the band at 810 cm^{-1} is ascribed to the out-of plane bending modes of C–N hetero-cycles. The bands at 1251, 1314, 1425, 1569 and 1637 cm^{-1} are attributable to aromatic C–N stretching and C=N stretching vibration mode [29,30]. For g-C₃N₄@BiVO₄ and g-C₃N₄@Ag/BiVO₄ samples, the main characteristic peaks of g-C₃N₄ and BiVO₄ are observed, suggesting the successfully loading of g-C₃N₄ in BiVO₄ system, which further validates the results of XRD.

To visually investigate the morphology and the detailed structure of the prepared samples, and then to deduce the formation process of the g-C₃N₄@Ag/BiVO₄ hybrid photocatalyst, the SEM images of synthesized photocatalysts were conducted, as shown in Fig. 4. The BiVO₄ particles exhibit decagon shape, where these well-fined crystals show smooth surface and relatively sharp edges (Fig. 4a). The top and bottom flat surfaces of the decagon shape are geometrically assigned as (040) facets, while the sides are defined as (110) facets according to the Li' report [24]. It has been certified that the good charge separation existed between the (040) and (110) facets, owing to the different energy levels of the conduction bands and valence bands for the two facets and the internal electronic field in a crystal. The photogenerated electrons and holes tend to accumulate on the (040) and (110) facets, respectively. It could be deduced that Ag⁺ particles were selectively reduced to metallic Ag and deposited on the (040) facets of BiVO₄ as shown in Fig. 4b. For a closer observation from the magnified SEM image of (040) facets of BiVO₄ shown in Fig. 4c, it can be clearly seen that the raised Ag particles are dispersed on the surface of (040) facets of BiVO₄. The corresponding elemental mapping images also exhibit the well dispersion of element Ag on the BiVO₄ (040) facets, which suggests that Ag was successfully reduced and deposited on the BiVO₄ (040) facets. The morphology of synthetic g-C₃N₄ is floccular (Fig. S4), which easily contact with other samples in the synthetic process of composite materials. After the introduction of g-C₃N₄ into the Ag/BiVO₄ (040) system, it can be observed that Ag/BiVO₄ (040) is covered by the floccular g-C₃N₄ to form a “sandwich” g-C₃N₄@Ag/BiVO₄ hybrid photocatalyst (Fig. 4d). The Ag nanoparticles, BiVO₄ (040) facets and floccular g-C₃N₄ keep intact morphology during the synthesis process, which can be seen from the magnified “sandwich” composite sample in Fig. 4e. Thus based on the above results, the synthetic process of the g-C₃N₄@Ag/BiVO₄ hybrid photocatalyst is able to be deduced and the schematic illustration is displayed in Fig. 4f.

The specific surface area values of BiVO₄, Ag/BiVO₄, g-C₃N₄, g-C₃N₄@BiVO₄ and g-C₃N₄@Ag/BiVO₄ were measured. The values are

0.57, 0.78, 43.02, 16.45, $20.82\text{ m}^2\text{g}^{-1}$, respectively. Combined with the dark reaction, the surface area values in these photocatalysts are not positively correlated with the dark adsorption. Obviously, the photocatalytic performance of the synthesized samples is not dependent on the surface area values, which is in line with Hu's reports [31].

Further evidence for the existence of the chemical compositions and electrons environment on the surface of the as-prepared samples derived from XPS analysis. Fig. 5 provides the XPS spectra of BiVO₄ (A₁), Ag/BiVO₄ (A₂), g-C₃N₄ (A₃) and g-C₃N₄@Ag/BiVO₄ (A₄). The XPS survey spectra (Fig. S5) of the four samples display the presence of Ag, Bi, V and N in g-C₃N₄@Ag/BiVO₄ composite, which can confirm the presence of g-C₃N₄ and Ag/BiVO₄ in the composite. Fig. 5a–f shows the high resolution spectrum of C 1s, N 1s, Bi 4f, V 2p, Ag 3d and O 1s, respectively. The samples containing g-C₃N₄ has three C 1s peaks (Fig. 5a) located at ca. 284.6, 286.1 and 287.9 eV. The peak located at 284.6 eV is attributed to adventitious carbon [3]. The peaks at 286.1 and 287.9 eV are assigned as C=N group and C–N or C–(N)₃ group of g-C₃N₄ [17,32]. The C 1s spectrum for g-C₃N₄@Ag/BiVO₄ is similar to that of g-C₃N₄, but the peak position of C–N or C–(N)₃ shifts towards lower binding energies. The regional spectrum of N 1s peak of g-C₃N₄ is depicted in Fig. 5b. The spectrum shows two peaks that are attributed to C=N–C at 398.7 and N–C₃ at 400.4 eV [32–34]. As for g-C₃N₄@Ag/BiVO₄ hybrid sample, the two peaks also shift to lower binding energies. Two peaks of pure BiVO₄ (Fig. 5c) at 159.2 and 164.5 eV are assigned to Bi 4f_{7/2} and Bi 4f_{5/2} induced by Bi³⁺ species [35,36]. The positions of the two peaks have not changed after Ag was deposited on BiVO₄ (040) facets, while increase to 159.4 and 164.7 eV after the addition of g-C₃N₄. The V 2p shows the peaks at 516.9 and 524.3 eV (Fig. 5d), which are attributed to V⁵⁺ of BiVO₄ particles [35,36]. Similarly, the peaks of V 2p in Ag/BiVO₄ composite are consistent with that of pure BiVO₄, but shift up to 517.0 and 524.5 eV in g-C₃N₄@Ag/BiVO₄. The Ag 3d peaks at 368.2 and 374.2 eV (Fig. 5e) are attributed to Ag⁰, suggesting the existence of metallic Ag nanoparticles on the surface of BiVO₄ sample [37,38]. The Ag peaks in g-C₃N₄@Ag/BiVO₄ do not changed compared with Ag/BiVO₄. The O 1s peak centered at 530.0 eV in Fig. 5f is associated with the V–O of BiVO₄, shifts to 530.1 eV in g-C₃N₄@Ag/BiVO₄ composite photocatalyst [35,36]. The other O 1s peak is assigned as –OH group or chemisorbed water molecule on the surface, and the content increases with the introduction of g-C₃N₄ in g-C₃N₄@Ag/BiVO₄ sample, which will favor the generation of O₂ or free radicals in the following photocatalytic oxidation process. It is obviously obtained that after the introduction of g-C₃N₄ in Ag/BiVO₄ system, the binding energies of Bi, V and O shift positively. And the binding energies of C and N in g-C₃N₄@Ag/BiVO₄ shift negatively with respect to pure g-C₃N₄. It was well known that the positive moving of binding energies represents lower electron density on the surface of photocatalyst. Correspondingly, the negative moving means higher electron density on the surface of photocatalyst. In addition, the binding energies of Ag remained unchanged in this process. It could be deduced that the electrons on BiVO₄ surface decrease and electrons on g-C₃N₄ surface increase for g-C₃N₄@Ag/BiVO₄ photocatalyst. For BiVO₄ photocatalyst, the valence band is composed of Bi 6s and O 2p orbits, and the conduction band is contributed by V 3d [39]. For g-C₃N₄, the valence band is made up of N 2p orbit, and the conduction band consists of C 2p and N 2p [33]. The BiVO₄ and g-C₃N₄ belongs to the semiconductor materials and the electrons in their valence bands can also be excited by X-ray in the XPS testing process. That is to say, the valence band (E_{VB}) electrons of pure BiVO₄ or g-C₃N₄ are excited to conduction band (E_{CB}), respectively. Owing to that the electrons on Ag surface located in the middle of the “sandwich” are unchanged, the decrease of electrons on BiVO₄ and increase of electrons on g-C₃N₄ surface might have interaction on Ag metallic phase to achieve the charge balance. It will be further stated in PL spectrum.

The UV–vis absorption spectrum of the as-synthesized samples is shown in Fig. 6a. It can be clearly seen that all the samples show strong absorption in the visible light region, and simultaneously each sample

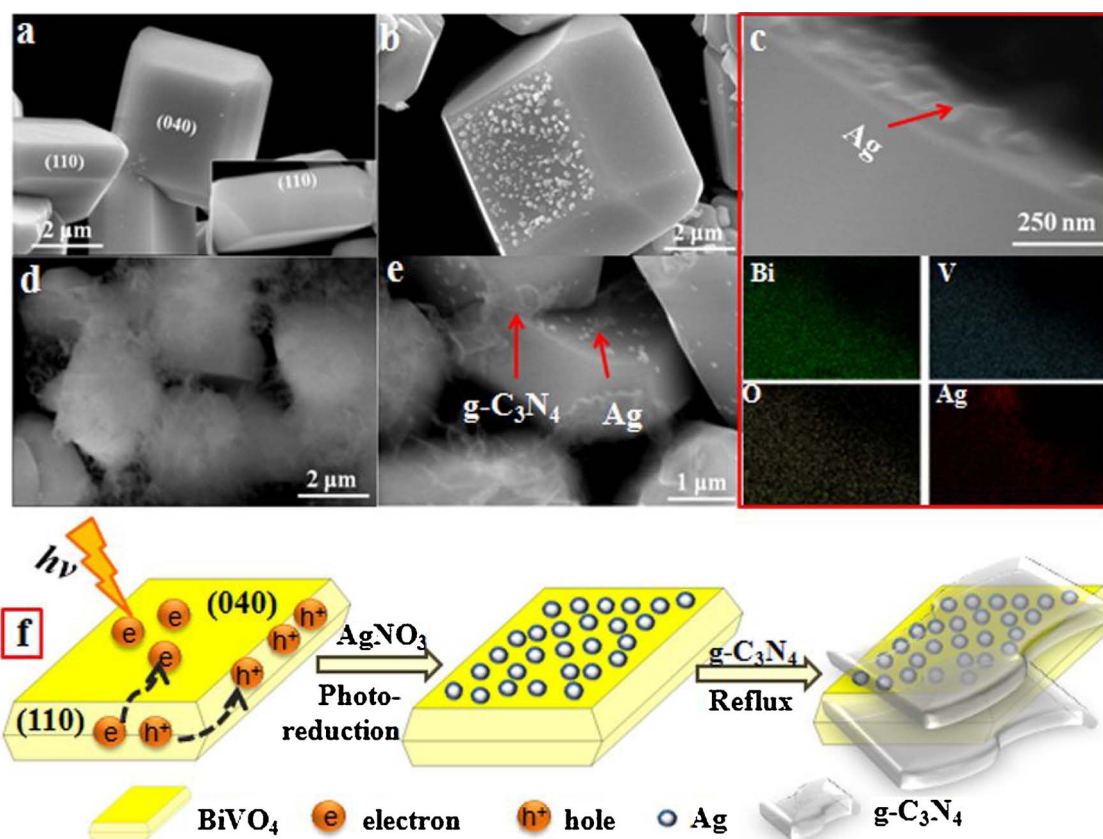


Fig. 4. SEM images and element distribution images and synthesis procedure of the photocatalysts. The typical SEM images of the as-synthesized (a) BiVO₄; (b) Ag/BiVO₄; (c) magnified Ag/BiVO₄ and its element mapping images for Bi, V, O and Ag; (d) and (e) g-C₃N₄@Ag/BiVO₄ photocatalysts; (f) Schematic illustration for the formation process of the Z-scheme g-C₃N₄@Ag/BiVO₄ photocatalysts.

exhibits the different absorption profile. Curves 6a and 6b display the UV–vis absorption spectrum of pure BiVO₄ and Ag/BiVO₄, respectively. Pure BiVO₄ has an absorption edge at about 550 nm, while Ag/BiVO₄ exhibits a resonance peak at approximately 620 nm with a small red shift and a better increase in visible absorption. The reason for this is due to that metallic Ag⁰ species was deposited on the crystal facet of BiVO₄ (040) and then cause the surface plasma resonance effect (SPR) [21]. Curve 6e shows the UV–vis absorption spectrum of pure g-C₃N₄ synthesized by supramolecular method with a strong absorption edge. The UV–vis absorption spectrum of g-C₃N₄@BiVO₄ and g-C₃N₄@Ag/BiVO₄ are displayed in curves 6c and 6d, respectively. In contrast to pure g-C₃N₄, the absorption edge of g-C₃N₄@BiVO₄ is weaker because of the presence of BiVO₄. The absorption edge of g-C₃N₄@Ag/BiVO₄ is between the pristine g-C₃N₄ and Ag/BiVO₄, which is attributed to that some g-C₃N₄ formed on the surface of Ag nanoparticles and then impeding the SPR effect of Ag⁰. Previous literature reported that the photoabsorption capability of photocatalyst affected the photoactivity, and other factors such as the effective active sites and the separation efficiency of photoinduced electron-hole pairs were also important to evaluate the photocatalytic performance [21].

On the account of that both BiVO₄ [20] and g-C₃N₄ [40] are direct band gap semiconductors, the band gaps of the pure materials are estimated by the plot of $(ah\nu)^2$ versus photo energy ($h\nu$) (Fig. 6b). The calculated band gap (E_g) of BiVO₄ is 2.28 eV. And the E_g value of g-C₃N₄ is 1.63 eV. Shalom et al. reported that the E_g value could shift from 2.25 to 1.55 eV when bulk g-C₃N₄ turned into fiber-type morphology g-C₃N₄ [41]. The band structure of g-C₃N₄ and BiVO₄ can be estimated according to the Mott-Schottky (MS) measurements, as shown in Fig. 7. The positive slopes indicate that both the two samples are n-type semiconductors. The flat band potential (V_{fb}) of BiVO₄ shown in Fig. 7a, as represented by the x-intercept of the linear region, is found to be

−0.59 V (vs Ag/AgCl at pH 6.8) and is very similar to the value measured by K. Sayama et al. for BiVO₄ electrode in 0.5 mol/L Na₂SO₄ solution. The V_{fb} of g-C₃N₄ is estimated to be −0.99 V under the identical conditions in Fig. 7b. The potential V_{fb} value is converted to RHE (reversible hydrogen electron) potentials using $E(RHE) = E(Ag/AgCl) + 0.059 \times pH + 0.197 V$ [42]. Therefore, the V_{fb} value for BiVO₄ and g-C₃N₄ is −0.01 and −0.39 V vs. RHE, respectively. In addition, V_{fb} is strongly related to the bottom of the E_{CB} of n-type semiconductor. In general, the E_{CB} relies on the electron effective mass and the carrier concentration and is considered to be located just 0 – 0.2 V more negative of the V_{fb} [43]. According to the above results, the band structure of g-C₃N₄ and BiVO₄ is able to be speculated and shown in Fig. 10.

Photoluminescence (PL) technique is widely used to investigate the charge transfer and recombination behaviour of the synthesized sample, and further to understand the process of electron-hole pairs in semiconducting samples. It is well known that the PL emission spectrum derive from the combination of photoinduced electron-hole pairs that can release energy. Generally, a lower PL intensity indicates a lower recombination of electron-hole pairs, thus leading to a higher photocatalytic performance. Fig. 8 displays PL spectrum of g-C₃N₄, g-C₃N₄@BiVO₄ and g-C₃N₄@Ag/BiVO₄ samples. As seen in the figure, the PL peak at about 460 nm of pure g-C₃N₄ is conducted, which is ascribed to the photogenerated charge carriers radiative recombination of self-trapped excitation on g-C₃N₄ surface [20]. Compared with that of g-C₃N₄, the PL intensity of g-C₃N₄@BiVO₄ composite is lower, suggesting that the recombination of photogenerated electron-hole pairs becomes relatively lower when the g-C₃N₄@BiVO₄ heterojunction is formed. However, it is interesting to observe that the g-C₃N₄@Ag/BiVO₄ sample with the best photoactivity does not show the lowest PL intensity. According to the foregoing description that the metallic Ag was deposited

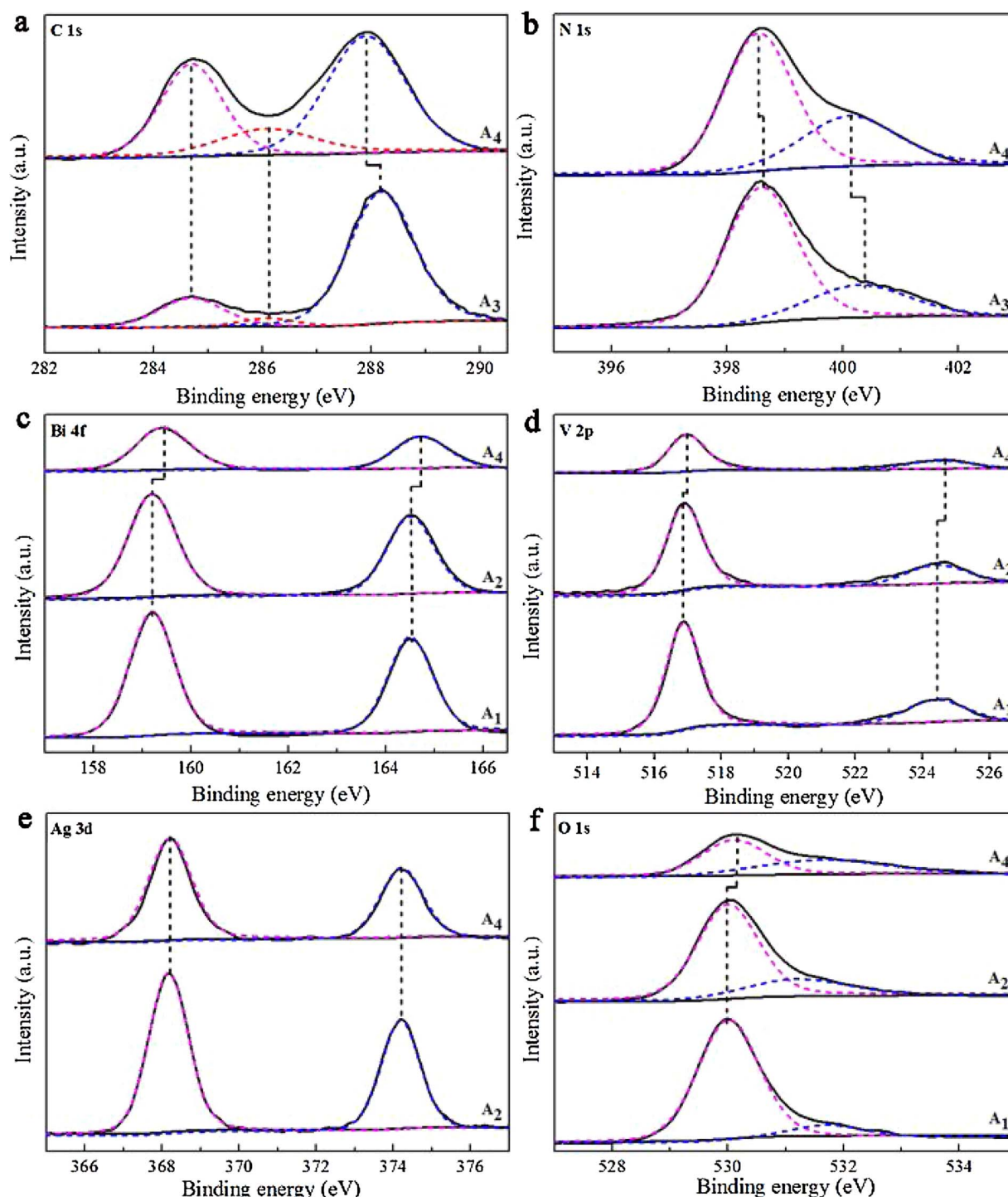


Fig. 5. XPS spectra of BiVO₄ (A₁), Ag/BiVO₄ (A₂), g-C₃N₄ (A₃) and g-C₃N₄@Ag/BiVO₄ (A₄) photocatalysts. (a) C 1s, (b) N 1s, (c) Bi 4f, (d) V 2p, (e) Ag 3d and (f) O 1s.

on the surface of BiVO₄ and g-C₃N₄ possesses suitable band position, it is preliminarily speculated that the photogenerated electrons in the CB of BiVO₄ and the holes in the VB of g-C₃N₄ may shift to the metallic Ag simultaneously and then combine on the surface of Ag. Therefore, it can be speculated that the higher recombination rate is occurred on the metallic Ag. The recombination of photoinduced charge carriers on metallic phase Ag is conducive to accelerate the separation of the photoinduced electron-hole pairs in both BiVO₄ and g-C₃N₄, which will improve the photocatalytic performance. Similar reports have been mentioned in Ag₃PO₄/Ag/SiC photocatalyst [18]. The increased PL signal for g-C₃N₄@Ag/BiVO₄ photocatalyst can be regarded as strong

evidence for a typically Z-scheme photocatalyst rather than a heterojunction photocatalyst. It can be indicated that rich electrons in the CB of BiVO₄ and holes in the VB of g-C₃N₄ participating the photocatalytic reactions.

The separation efficiency of photoinduced electron-hole pairs is also important to influence the photocatalytic performance. The photocurrent response (*i-t*) curves with or without visible-light irradiation were used to evaluate the separation efficiency of photoinduced electron-hole pairs of the photocatalysts [44,45]. As shown in Fig. 9a, the g-C₃N₄@Ag/BiVO₄ photocatalyst displays the highest photocurrent intensity. The photo-current density of g-C₃N₄@Ag/BiVO₄ composite

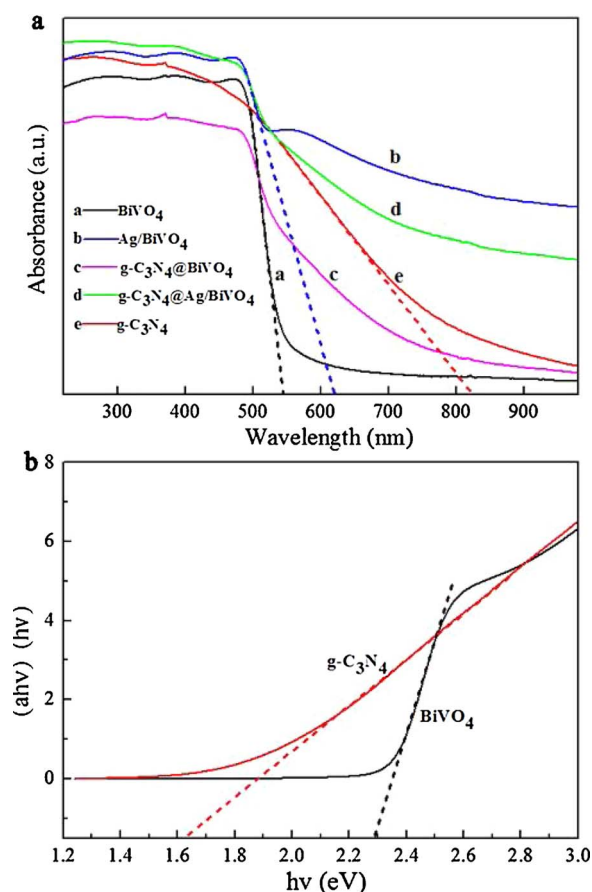


Fig. 6. (a) UV-vis diffuse reflection spectra patterns of the as-synthesized BiVO₄, Ag/BiVO₄, g-C₃N₄@BiVO₄, g-C₃N₄@Ag/BiVO₄ and pure g-C₃N₄; (b) The plot of $(\alpha h\nu)^2$ versus photo energy ($h\nu$) for pure BiVO₄ and g-C₃N₄.

($2.08 \mu\text{A cm}^{-2}$) is 6.3 times higher than that of pure g-C₃N₄ ($0.33 \mu\text{A cm}^{-2}$), 5.5 times of pure BiVO₄ ($0.38 \mu\text{A cm}^{-2}$), 3.2 times of Ag/BiVO₄ ($0.65 \mu\text{A cm}^{-2}$) and 2.3 times of g-C₃N₄@Ag/BiVO₄ ($0.89 \mu\text{A cm}^{-2}$). It demonstrates that the g-C₃N₄@Ag/BiVO₄ sample exhibits better interfacial charge transfer and higher efficiency in separating and migrating of photogenerated charge carriers after the introduction of metallic Ag and g-C₃N₄ in BiVO₄ system. Electrochemical impedance spectrum (EIS) measurements in Fig. 9b were conducted to investigate the charge transfer resistance and the separation efficiency of the photoinduced charge carriers [44]. The diameter for arc radius of pure g-C₃N₄, pristine BiVO₄, Ag/BiVO₄, g-C₃N₄@BiVO₄ and g-

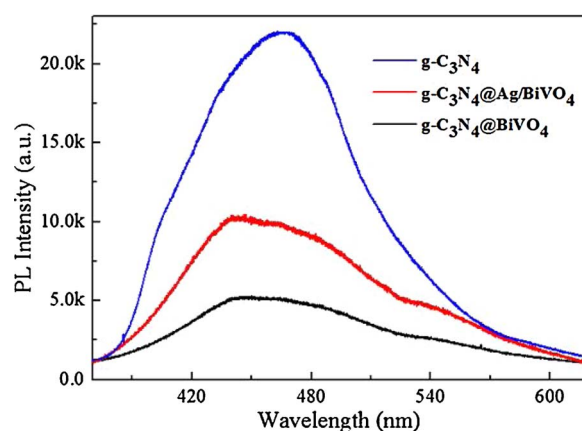


Fig. 8. Photoluminescence spectra of as-synthesized g-C₃N₄, g-C₃N₄@BiVO₄ and g-C₃N₄@Ag/BiVO₄ photocatalysts.

C₃N₄@Ag/BiVO₄ photocatalysts appears a decline trend. The diameter for arc radius of g-C₃N₄@Ag/BiVO₄ electrode is the smallest. It indicates a decrease in the charge-transfer resistance on g-C₃N₄@Ag/BiVO₄ surface and thus leading to an effective electron-hole pair separation, which is consistent with that of *i-t* results. The above results confirm that the g-C₃N₄@Ag/BiVO₄ photocatalyst possesses the highest separation and migration efficiency of photogenerated charge carriers during the process of photocatalytic reaction, which will promote the improvement of the photocatalytic performance. In addition, for the BiVO₄ modified by the different content of metallic Ag, the *i-t* curves and EIS were also performed (Fig. S6a₁ and b₁). The 2 wt% Ag/BiVO₄ shows the highest photogenerated electron-holes separation efficiency in the three samples. After the different concentration of g-C₃N₄ covered the Ag/BiVO₄ (2 wt% Ag/BiVO₄), the separation efficiency of photogenerated electron-hole pairs increases firstly and then decreases, of which the g-C₃N₄@Ag/BiVO₄ (100% g-C₃N₄@Ag/BiVO₄) is the largest, as shown in Fig. S6a₂ and b₂. The above results are well consistent with that of photocatalytic performance.

3.3. Mechanism analysis of the photocatalytic oxidation

The photocatalytic test indicated that the g-C₃N₄@Ag/BiVO₄ composite photocatalyst displayed excellent photocatalytic oxidation activity. If g-C₃N₄ and Ag/BiVO₄ have form a conventional heterojunction, then, under the visible light irradiation, the photoinduced electrons tend to transfer from the CB of g-C₃N₄ to that of Ag/BiVO₄, and the holes tend to transfer from the VB of Ag/BiVO₄ to that of g-C₃N₄. Owing to the lower position of the VB of g-C₃N₄, the photocatalytic oxidation

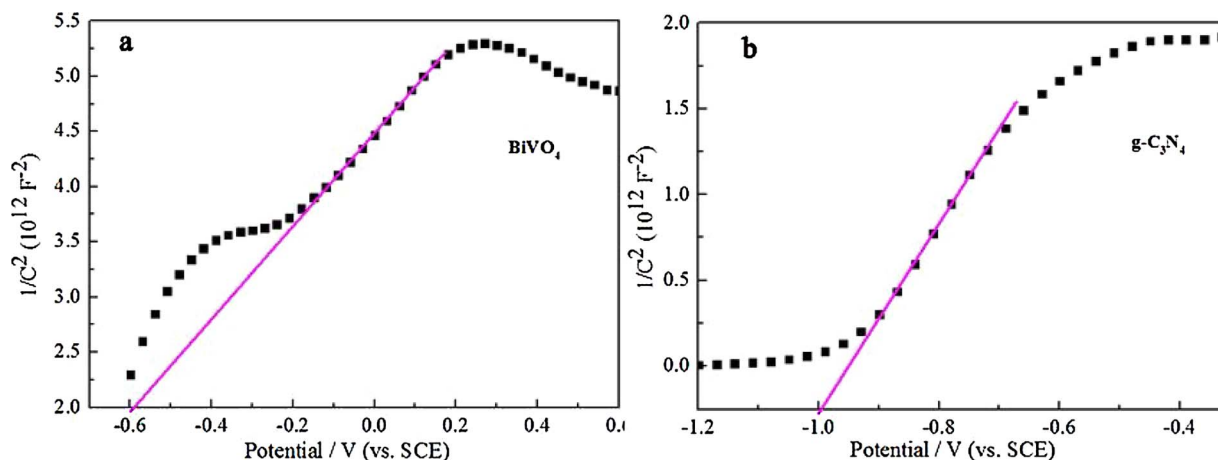


Fig. 7. Mott-Schottky (MS) plots of (a) pure BiVO₄ and (b) pure g-C₃N₄ electrodes.

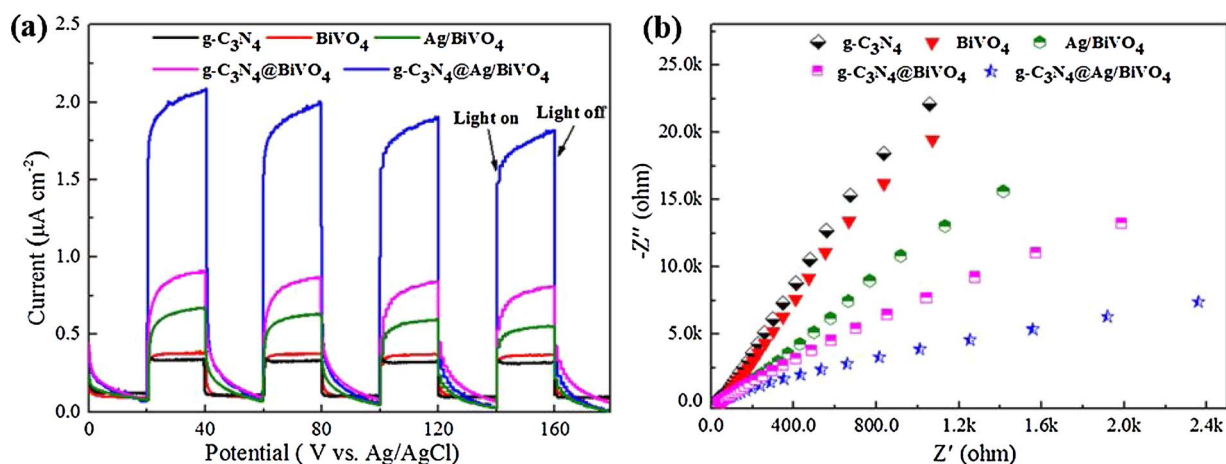


Fig. 9. I-t (a) and EIS (b) spectra of as-synthesized $\text{g-C}_3\text{N}_4$, BiVO_4 , Ag/BiVO_4 , $\text{g-C}_3\text{N}_4@\text{BiVO}_4$ and $\text{g-C}_3\text{N}_4@\text{Ag/BiVO}_4$ photocatalysts.

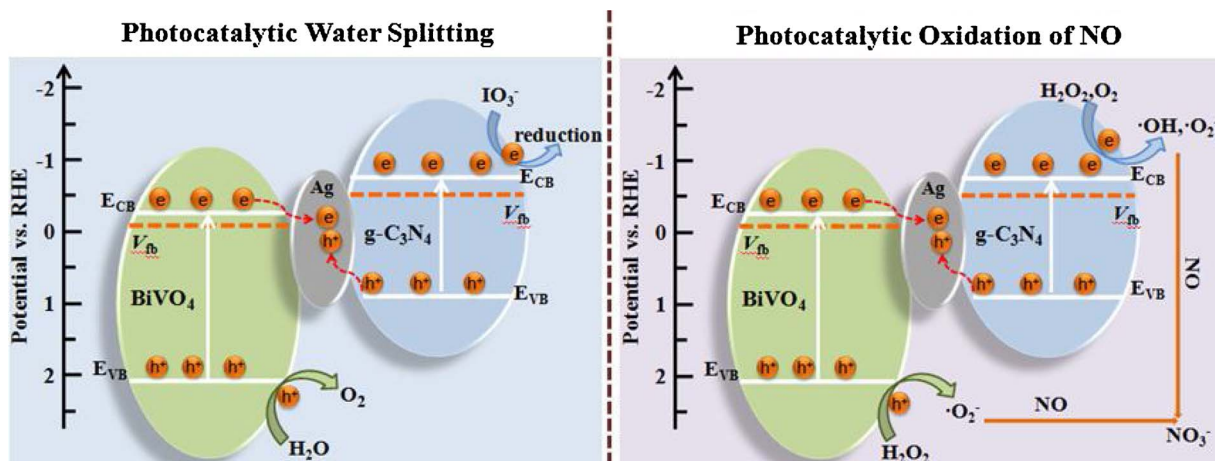


Fig. 10. The energy band diagram and the proposed Z-scheme schematic description of the mechanism for the $\text{g-C}_3\text{N}_4@\text{Ag/BiVO}_4$ photocatalyst on the photocatalytic oxidation of water and NO under visible light irradiation, respectively.

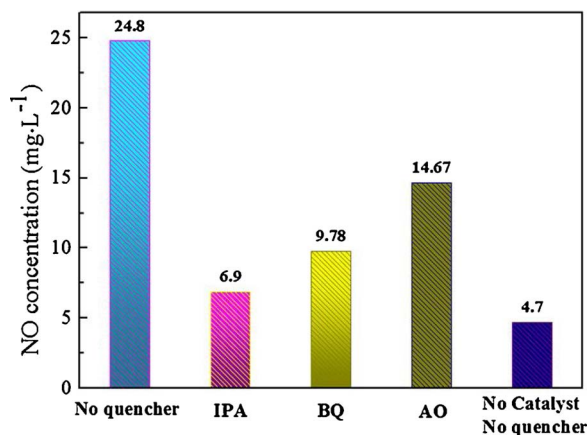


Fig. 11. Trapping experiment of active species during the photocatalytic oxidation of NO over $\text{g-C}_3\text{N}_4@\text{Ag/BiVO}_4$ sample under visible light irradiation.

efficiency could not be as high as that of the experimental results. Therefore, it suggested that the transfer of photoinduced electrons and holes in the $\text{g-C}_3\text{N}_4@\text{Ag/BiVO}_4$ hybrids followed the Z-scheme system with Ag as electron mediator.

On the basis of the above characterization and experimental results, the possible mechanism of Z-scheme $\text{g-C}_3\text{N}_4@\text{Ag/BiVO}_4$ hybrid photocatalyst is shown in Fig. 10. Under visible light irradiation, both $\text{g-C}_3\text{N}_4$ and BiVO_4 are excited, and then photoexcited electrons and holes

are in their CB and VB, respectively. Here the metal Ag was directly photodeposited on the (040) facets of BiVO_4 and also act as a charge carriers recombination center in Z-scheme $\text{g-C}_3\text{N}_4@\text{Ag/BiVO}_4$ system. Therefore, the electrons on the CB of BiVO_4 can flow into metal Ag through the Schottky barrier due to that the CB of BiVO_4 is more negative than that Fermi level of Ag nanoparticles. The electrons will store in the lowest unoccupied orbital of Ag and thus elevating the Fermi level of Ag, which has also been reported by Wu et. al [21]. In order to maintain the Fermi level of Ag equilibrium again, the photogenerated holes from $\text{g-C}_3\text{N}_4$ will be quickly transferred to Ag. That is to say, the photogenerated electron on the CB of BiVO_4 and holes on the VB of $\text{g-C}_3\text{N}_4$ could annihilate at metal Ag nanoparticles, which corresponds to the PL results. Subsequently, the strong reductive electrons would be left on the CB of $\text{g-C}_3\text{N}_4$, and the strong oxidizing holes would be left on the VB of BiVO_4 . This will contribute to the separation of photo-generated electron-hole pairs and then accelerating the photocatalytic performance. For photocatalytic water splitting to produce O_2 reaction, the photogenerated holes were probably involved in water oxidation and the electrons were involved in the reduction of IO_3^- . For PCO of NO reaction, the photogenerated electrons and holes would react with active substances (O_2 , H_2O_2) to produce major free radicals ($\cdot\text{OH}$, $\cdot\text{O}_2^-$) with strong oxidizing property, which has been analyzed in our previous paper [3,4]. In $\text{g-C}_3\text{N}_4@\text{Ag/BiVO}_4$ Z-scheme, we also conduct a trapping experiment to confirm the determined free radical in PCO of NO and the concrete experimental process is as follows: Five quartz tubes filled with 40 mL deionized water and 4 mL 30% H_2O_2 solution were divided into four experimental groups (a–d) and the control group

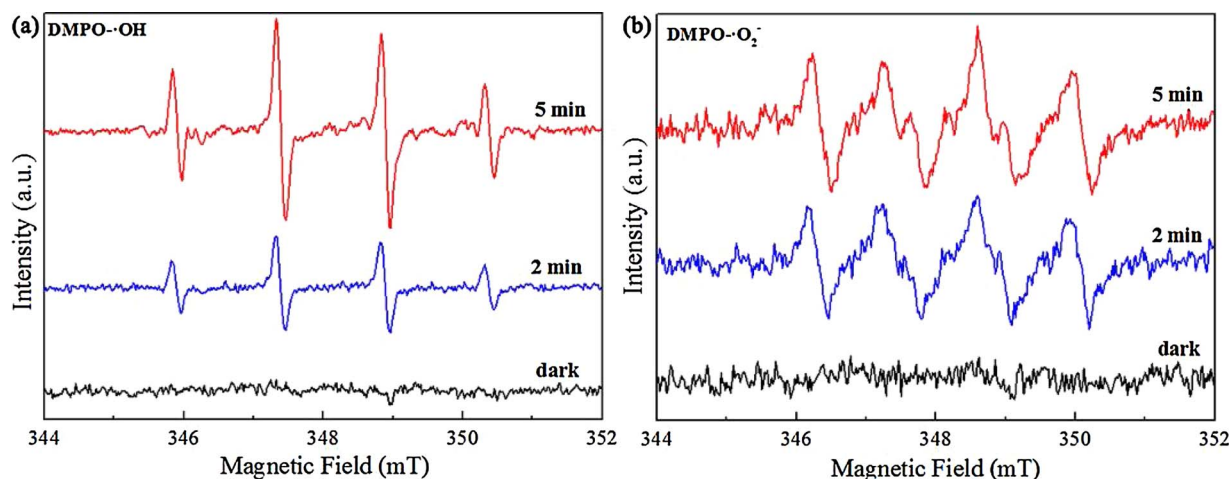


Fig. 12. (a) DMPO spin-trapping ESR spectra in $g\text{-C}_3\text{N}_4\text{@Ag/BiVO}_4$ dispersion in dark or under visible light irradiation: (a) in aqueous dispersion for $\text{DMPO}\cdot\text{OH}$ and (b) in methanol dispersion for $\text{DMPO}\cdot\text{O}_2^{\cdot-}$.

(e). 10 mg $g\text{-C}_3\text{N}_4\text{@Ag/BiVO}_4$ sample was added into each experimental group, respectively. Subsequently, 1 mL isopropyl alcohol (IPA), 0.1 mmol *p*-benzoquinone (BQ) and 0.1 mmol ammonium oxalate (AO), as the scavenger of hydroxyl radicals ($\cdot\text{OH}$), superoxide radicals ($\cdot\text{O}_2^{\cdot-}$) and holes (h^+), was injected into group (b)–(d), respectively [46–48]. Then NO was introduced via the gas distributor and all quartz tubes were exposed to visible light irradiation for 30 min in stirring condition. After the clear supernatant was obtained by centrifugation and then injected into IC. The trapping experiment process has also been illustrated in our previous papers [3,4]. IC Quantitative analysis displays that the NO_3^- concentration of the experimental group (a)–(d) as well as the control group (e) is 24.8, 6.9, 9.78, 14.67 and 4.70 mg L^{-1} , respectively, as shown in Fig. 11. Here, experimental group (b)–(d) contains the scavenger of $\cdot\text{OH}$, $\cdot\text{O}_2^{\cdot-}$ and h^+ , respectively and control group (e) is conducted with the absence of photocatalyst. It is obtained that $\cdot\text{OH}$, $\cdot\text{O}_2^{\cdot-}$ and h^+ are the efficient free radicals in the PCO of NO in $g\text{-C}_3\text{N}_4\text{@Ag/BiVO}_4$ Z-scheme photocatalyst. The order to contributing to the PCO of NO is $\cdot\text{OH} > \cdot\text{O}_2^{\cdot-} > h^+$ and $\cdot\text{OH}$ plays a pivotal role. In order to further validate the active species generation in the photocatalytic system under visible light irradiation, the ESR spin-trap with 5,5-dimethyl-1-pyrroline N-oxide (DMPO) technique was also performed over $g\text{-C}_3\text{N}_4\text{@Ag/BiVO}_4$ composite. The detection of the generation of $\text{DMPO}\cdot\text{OH}$ was performed as follows 100 μL DMPO, 1 mL ultrapure water and 5 mg samples. And $\text{DMPO}\cdot\text{O}_2^{\cdot-}$ was conducted in 1 mL methanol dispersion and other factors remained unchanged. All the experiments were conducted under dark condition and visible light irradiation of 2 min and 5 min, which is shown in Fig. 12. From Fig. 12a, four characteristic peaks of $\text{DMPO}\cdot\text{OH}$ are investigated in aqueous solution with the visible light on, but the signals do not find at dark condition. Notably, stronger intensity $\text{DMPO}\cdot\text{OH}$ are observed with the time increased from 2 min to 5 min, suggesting that $\cdot\text{OH}$ plays a vital role for the improved photocatalytic performance. As depicted in Fig. 12b, the signals of $\text{DMPO}\cdot\text{O}_2^{\cdot-}$ are observed in methanol solution when exposed to the visible light. Thus the $\cdot\text{O}_2^{\cdot-}$ is proved to be generated in the photocatalytic process. However, the peaks intensity only increases a little bit from the irradiation from 2 min to 5 min. Hence, the ESR analysis reveals that the generation of $\cdot\text{OH}$ and $\cdot\text{O}_2^{\cdot-}$ in the photocatalytic process promote the photocatalytic oxidation performance, and $\cdot\text{OH}$ plays a dominant role, which is consistent with that reported in trapping experiment.

4. Conclusions

In our work, the high-efficiency hierarchically Z-scheme $g\text{-C}_3\text{N}_4\text{@Ag/BiVO}_4$ (040) hybrid photocatalyst were fabricated via a

facile two-step method. Through this approach, $g\text{-C}_3\text{N}_4\text{@Ag/BiVO}_4$ (040) composite with the exposed photogenerated electron-rich (040) facets, Ag as transmission electronic medium and flocculent $g\text{-C}_3\text{N}_4$ to form the heterojunction could be intuitively investigated by SEM. Compared with pure BiVO_4 sample, the Z-scheme system exhibits a higher photoefficiency on both the photocatalytic water splitting and the PCO of NO. The origin of the distinctly excellent photocatalytic performance of the $g\text{-C}_3\text{N}_4\text{@Ag/BiVO}_4$ (040) mainly attributed to the highly separation rate of photo-induced charge carriers in the Z-scheme heterojunction system, which is illustrated by XPS and PL spectra. Herein, the metal Ag nanoparticles act as the electron mediator to conduct the electrons from BiVO_4 to metal Ag and then attract holes from $g\text{-C}_3\text{N}_4$ to Ag surface to make the Ag electron environmental equilibrium. Moreover, in the PCO of NO process, $\cdot\text{OH}$ and $\cdot\text{O}_2^{\cdot-}$ are generated and $\cdot\text{OH}$ plays a dominant role.

Acknowledgements

Information Ministry of the People's Republic of China 2012 (543), the National Natural Science Foundation of China (51408309 and 51578288), Science and Technology Support Program of Jiangsu Province (BE2014713), Natural Science Foundation of Jiangsu Province (BK20140777), Industry-Academia Cooperation Innovation Fund Projects of Jiangsu Province (BY2014004-10), Science and technology project of Nanjing (201306012), Jiangsu Province Scientific and Technological Achievements into a Special Fund Project (BA2015062), A Project Funded by the Priority Academic Program Development of Jiangsu Higher Education of Jiangsu Higher Education Institutions.

Appendix A. Supplementary data

Supplementary data associated with this article can be found, in the online version, at <http://dx.doi.org/10.1016/j.apcatb.2017.09.005>.

References

- [1] M. Tabata, K. Maeda, M. Higashi, D. Lu, T. Takata, R. Abe, K. Domen, *Langmuir* 26 (2010) 9161–9165.
- [2] J.J. Xian, D.Z. Li, J. Chen, X.F. Li, M. He, Y. Shao, L.H. Yu, J.L. Fang, *ACS Appl. Mater. Interfaces* 6 (2014) 13157–13166.
- [3] M. Ou, H.Y. Nie, Q. Zhong, S.L. Zhang, L. Zhong, *Phys. Chem. Chem. Phys.* 17 (2015) 28809–28817.
- [4] M. Ou, Q. Zhong, S.L. Zhang, H.Y. Nie, Z.J. Lv, W. Cai, *Appl. Catal. B: Environ.* 193 (2016) 160–169.
- [5] J. Xu, W.Z. Wang, J. Wang, Y.J. Liang, *Appl. Surf. Sci.* 349 (2015) 529–537.
- [6] A. Fujishima, K. Honda, *Nature* 238 (1972) 37–38.
- [7] Z.H. Ai, W.K. Ho, S.C. Lee, *J. Phys. Chem. C* 115 (2011) 25330–25337.
- [8] D.G. Wang, H.F. Jiang, X. Zong, Q. Xu, Y. Ma, G.L. Li, C. Li, *Chemistry* 17 (2011)

- 1275–1282.
- [9] M. Wang, Q. Liu, Y.S. Che, L.F. Zhang, D. Zhang, *J. Alloys Compd.* 548 (2013) 70–76.
- [10] Y.Z. Wang, W. Wang, H.Y. Mao, Y.H. Lu, J.G. Lu, J.Y. Huang, Z.Z. Ye, B. Lu, *ACS Appl. Mater. Interfaces* 6 (2014) 12698–12706.
- [11] S.Y. Dong, Y.Q. Cui, Y.F. Wang, Y.K. Li, L.M. Hu, J.Y. Sun, J.H. Sun, *Chem. Eng. J.* 249 (2014) 102–110.
- [12] W.R. Zhao, Y. Wang, Y. Yang, J. Tang, Y.N. Yang, *Appl. Catal. B: Environ.* 115–116 (2012) 90–99.
- [13] F. Chen, Q. Yang, X.M. Li, G.M. Zeng, D.B. Wang, C.G. Niu, J.W. Zhao, H.X. An, T. Xie, Y.C. Deng, *Appl. Catal. B: Environ.* 200 (2017) 330–342.
- [14] A. Iwase, Y.H. Ng, Y. Ishiguro, A. Kudo, R. Amal, *J. Am. Chem. Soc.* 133 (2011) 11054–11057.
- [15] X.L. Yu, A. Shavel, X.Q. An, Z.S. Luo, M. Ibanez, A. Cabot, *J. Am. Chem. Soc.* 136 (2014) 9236–9239.
- [16] F. Jiang, T. Gunawan, Y.B. Harada, T. Kuang, K. Minegishi, K. Domen, S. Ikeda, *J. Am. Chem. Soc.* 137 (2015) 13691–13697.
- [17] W.Q. Zhao, L.H. Xie, M. Zhang, Z.Y. Ai, H.P. Xi, Y.J. Li, Q.M. Shi, J.S. Chen, *Int. J. Hydrogen Energy* 41 (2016) 6277–6287.
- [18] Z.H. Chen, F. Bing, Q. Liu, Z.G. Zhang, X.M. Fang, *J. Mater. Chem. A* 3 (2015) 4652–4658.
- [19] C.S. Pan, J. Xu, Y.J. Wang, D. Li, Y.F. Zhu, *Adv. Funct. Mater.* 22 (2012) 1518–1524.
- [20] M. Ou, Q. Zhong, S.L. Zhang, L.M. Yu, *J. Alloys Compd.* 626 (2015) 401–409.
- [21] H.Y. Li, Y.J. Sun, B. Cai, S.Y. Gan, D.X. Han, L. Niu, T.S. Wu, *Appl. Catal. B: Environ.* 170–171 (2015) 206–214.
- [22] F. Chen, Qi. Yang, L. Zhou, Y.L. Wang, J.W. Zhao, D.B. Wang, X.M. Li, Z. Guo, H. Wang, Y.C. Deng, C.G. Niu, G.M. Zeng, *Appl. Catal. B: Environ.* 205 (2017) 133–147.
- [23] X. Lin, D. Xu, Y. Xi, R. Zhao, L.N. Zhao, M.S. Song, H.J. Zhai, G.B. Che, L.M. Chang, *Colloids Surf.* 513 (2017) 117–124.
- [24] R.G. Li, H.X. Han, F.X. Zhang, D.G. Wang, C. Li, *Energy Environ. Sci.* 7 (2014) 1369–1376.
- [25] Z.B. Wu, Z.Y. Sheng, Y. Liu, H.Q. Wang, N. Tang, J. Wang, *J. Hazard. Mater.* 164 (2009) 542–548.
- [26] W.Z. Yin, W.Z. Wang, L. Zhou, S.M. Sun, L. Zhang, *J. Hazard. Mater.* 173 (2010) 194–199.
- [27] L.Q. Ye, J.Y. Liu, Z. Jiang, T.Y. Peng, L. Zan, *Appl. Catal. B: Environ.* 142–143 (2013) 1–7.
- [28] D.N. Ke, T.Y. Peng, L. Ma, P. Cai, K. Dai, *Inorg. Chem.* 48 (2009) 4689–4691.
- [29] H.J. Yan, H.X. Yang, *J. Alloys Compd.* 509 (2011) L26–L29.
- [30] M. Yang, Q. Huang, X.Q. Jin, *Mater. Sci. Eng. B* 177 (2012) 600–605.
- [31] X. Song, Y. Hu, M.M. Zheng, C.H. Wei, *Appl. Catal. B: Environ.* 182 (2016) 587–597.
- [32] S.C. Yan, Z.S. Li, Z.G. Zou, *Langmuir* 26 (2010) 3894–3901.
- [33] S.M. Wang, D.L. Li, C. Sun, S.G. Yang, Y. Guan, H. He, *Appl. Catal. B: Environ.* 144 (2014) 885–892.
- [34] H.W. Kang, S.N. Lim, D. Song, S.B. Park, *Int. J. Hydrogen Energy* 37 (2012) 11602–11610.
- [35] M. Wang, H.Y. Zheng, J. Liu, D. Dong, Y.S. Che, C.X. Yang, *Mater. Sci. Semicond. Process.* 30 (2015) 307–313.
- [36] P. Madhusudan, J. Ran, J. Zhang, J.G. Yu, G. Liu, *Appl. Catal. B: Environ.* 110 (2011) 286–295.
- [37] M.S. Zhu, P.L. Chen, M.H. Liu, *ACS Nano* 5 (2011) 4529–4536.
- [38] Y.X. Tang, Z.L. Jiang, G.C. Xing, A.Q. Li, P.D. Kanhere, Y.Y. Zhang, T.C. Sum, S.Z. Li, X.D. Chen, Z.L. Dong, Z. Chen, *Adv. Funct. Mater.* 23 (2013) 2932–2940.
- [39] Y.S. Fu, X.Q. Sun, X. Wang, *Mater. Chem. Phys.* 131 (2011) 325–330.
- [40] X.J. Wang, Q. Wang, F.T. Li, W.Y. Yang, Y. Zhao, Y.J. Hao, S.J. Liu, *Chem. Eng. J.* 234 (2013) 361–371.
- [41] Y. Ishida, L. Chabanne, M. Antonietti, M. Shalom, *Langmuir* 30 (2014) 447–451.
- [42] T. Tachikawa, T. Ochi, Y. Kobori, *ACS Catal.* 6 (2016) 2250–2256.
- [43] E.P. Gao, W.Z. Wang, M. Shang, J.H. Xu, *Phys. Chem. Chem. Phys.* 13 (2011) 2887–2893.
- [44] Y.Y. Bu, Z.Y. Chen, W.B. Li, *Appl. Catal. B: Environ.* 144 (2014) 622–630.
- [45] S. Kumar, T. Surendar, B. Kumar, A. Baruah, V. Shanker, *J. Phys. Chem. C* 117 (2013) 26135–26143.
- [46] W. Liu, M.L. Wang, C.X. Xu, S.F. Chen, *Chem. Eng. J.* 209 (2012) 386–393.
- [47] L.Q. Ye, J.Y. Liu, Z. Jiang, T.Y. Peng, L. Zan, *Appl. Catal. B: Environ.* 142–143 (2013) 1–7.
- [48] H.Y. Nie, M. Ou, Q. Zhong, S.L. Zhang, L.M. Yu, *J. Hazard. Mater.* 300 (2015) 598–606.